Supplementary Information (SI) for Chemical Science.

Supplementary Information

Understanding the strain effect in alkaline hydrogen oxidation reaction over well-defined Ru surfaces: Insights into catalyst design

Zihan Guo,[†a] Yan Qiao,[†a] Mengfan Li,[a] Zhenghe Gong,[b] Jingwei Yu,[a] Yanan Wang,[a] Liang Zhao,[a] Yang Li,[a] Zehua Hu,[*c] Yangfan Lu,[d] and Hongwen Huang[*a,b]

[a]College of Materials Science and Engineering, Hunan University, Changsha, Hunan 410082, P. R. China.

[b]Key Laboratory of Mesoscopic Chemistry of MOE and Jiangsu Provincial Lab for Nanotechnology, School of Chemistry and Chemical Engineering, Nanjing University, Nanjing, Jiangsu 210023, P. R. China.

[c]National Laboratory of Solid State Microstructures, School of Electronic Science and Engineering, and Collaborative Innovation Center of Advanced Microstructures, Nanjing University, Jiangsu 210023, P. R. China.

[d]School of Materials Science and Engineering, State Key Laboratory of Silicon and Advanced Semiconductor Materials, Zhejiang University, Hangzhou, Zhejiang 310027, P. R. China

[†]These authors contributed equally to this work.

Correspondence and requests for materials should be addressed to Z. H. (zehuahu@nju.edu.cn) or H.H. (huanghw@nju.edu.cn).

Experimental Section

Chemicals. Ruthenium (III) trichloride trihydrate ($RuCl_3 \cdot 3H_2O$, 98%) and diethylene glycol ($C_4H_{10}O_3$, >99%) were purchased from Shanghai Macklin Biochemical Co., Ltd. (Shanghai, China). Potassium bromide (KBr, AR), potassium hydroxide (KOH, AR), potassium chloride (KCl, AR), iron trichloride ($FeCl_3$, CP, ≥97.0%), formaldehyde (HCHO, AR), L-Ascorbic acid ($C_6H_8O_6$, AR), ethanol (CH_3CH_2OH, AR, ≥99.7%), ethylene glycol (CH_2OHCH_2OH, AR), sodium borohydride ($NaBH_4$, 98%), acetone (CH_3COCH_3, AR) and hydrochloric acid (HCl, 36.0%-38.0%) were purchased from Sinopharm Chemical Reagent Co., Ltd. (Shanghai China). Tetrachloropalladate (Na_2PdCl_4, 98%), Polyvinylpyrrolidone (PVP, M_w=55,000) and Nafion (5 wt.%) were purchased from Sigma-Aldrich Co., Ltd. The deionized water (18.2 MΩ/cm) used in all experiments was obtained from ultra-pure purification system (Master-515Q, HHitech). All the chemicals were used without further purification.

Characterizations. The X-ray diffraction (XRD) spectra were recorded using a powder X-ray diffractometer (Bruker D8 Advance) with a Cu Kα X-ray tube in the range from 20^o to 80^o at the scan rate of 10 $deg \cdot min^{-1}$. The morphology and structure of catalysts were investigated using a transmission electron microscopy (JEOL JEM-2100Plus) and high-angle annular dark-field scanning transmission electron microscopy (HAADF-STEM, Thermo scientific Themis Z 3.2) with a spherical aberration corrector. Elemental analysis of nanocatalysts was quantitatively determined by inductively coupled plasma-mass spectrometry (ICP-MS) using a SPECTRO BLUE SOP. X-ray photoelectron spectroscopy (XPS) spectra were collected by using a Thermo Scientific K-Alpha equipped with an Al Kα (hv=1486.6 eV) excitation source.

Synthesis of Pd icosahedra. In a typical synthesis, 105 mg of PVP was dissolved in 2 mL of diethylene glycol (DEG) and preheated at 120 °C for 10 min under magnetic stirring. Then, 1 mL of DEG solution containing Na_2PdCl_4 (15.5 mg mL^{-1}) was added in a single shot, and the reaction was allowed to proceed for 4 h. After cooling to room temperature, the solid products were collected by centrifugation at 13000 rpm using acetone, followed by washing twice with water at 15000 rpm. Finally, the Pd icosahedra were dispersed in ethylene glycol (EG) for further use.

Synthesis of Pd cubes. Pd nanocubes with an edge length of 6 nm were synthesized following the improved protocol.[1] In a typical synthesis, 105 mg of PVP, 60 mg of AA, 185 mg of KCl and 5 mg of KBr were dissolved in 8.0 mL of deionized (DI) water. The solution was then placed in a vial and pre-heated to 80 °C in an oil bath under magnetic stirring for 10 min. Subsequently, 3 mL of aqueous Na_2PdCl_4 solution (64.6 mM) was injected into the preheated solution in a single shot. The reaction was maintained at 80 °C under stirring for 3 h. After cooling naturally to room temperature, the product was collected by centrifugations, washed three times with DI water to remove excess PVP and inorganic ions, and then re-dispersed in 11 mL of ethylene glycol (EG).

Synthesis of Pd octahedra. Pd octahedra were synthesized following the method.[2] In a typical synthesis, 105 mg of PVP, 100 μL of HCHO, 0.3 mL of an aqueous suspension of the as-prepared Pd nanocubes and 7.7 mL of deionized (DI) water were mixed in a vial and pre-heated at 60 °C for 10 min under magnetic stirring. Then 3.0 mL of aqueous Na_2PdCl_4 solution (32.8 mM) was added to the pre-heated solution in one shot. After the vial was capped, the reaction was allowed to proceed at 60 °C for another 3 h. After collection by centrifugation and being washed three times with DI water at 15000 rpm, the final product was re-dispersed in 9 mL of ethylene glycol (EG).

Synthesis of Pd@Ru icosahedra. Pd@Ru icosahedra were synthesized following a standard procedure. In a typical synthesis, 8 mL of EG containing 50 mg of AA, 40 mg KBr, 105 mg PVP, and 0.9 mg of Pd icosahedral seeds were added into a Schlenk bottle and heated to 200 °C under magnetic stirring for 20 min. Then, 20 mL of EG containing 1.08 mg of $RuCl_3$ $3H_2O$ was titrated into the solution at a programmable rate of 1.0 mL h^{-1}. After the complete addition of the Ru (III) precursor, the reaction was allowed to continue for another 2 h. The solid products were collected by centrifugation, washed once with acetone and twice with ethanol, and finally dispersed in ethanol for further use.

Synthesis of Pd@Ru octahedra. In a typical synthesis, 8 mL of EG containing 40 mg of AA, 60 mg of KBr, 105 mg of PVP, and 0.9 mg of Pd octahedral seeds were added into a Schlenk bottle and heated to 200 °C under magnetic stirring for 20 min. Then, 20 mL of EG containing 1.2 mg of $RuCl_3$ $3H_2O$ was titrated into the solution at a rate of 1.0 mL h^{-1}. After the complete addition of the Ru (III) precursor, the reaction was allowed to continue for an additional 2 h. Afterwards, the solid products were collected by centrifugation, washed once with acetone and twice with ethanol, and then re-dispersed in ethanol for further use.

Fabrication of Ru octahedral or icosahedral nanocages. In a typical process, 30 mg $FeCl_3$, 0.1 mL of HCl, 50 mg of PVP, and 300 mg of KBr were dissolved in 4.9 mL of DI water and preheated to 90 °C for 5 min. Subsequently, aqueous solution of as-synthesized Pd@Ru octahedra or icosahedra (with a solid content of 0.3 mg) was added. The reaction was allowed to proceed for 1 h. The floating products on the surface were collected carefully by centrifugation, washed twice with water, and then re-dispersed in water for further use.

Synthesis of Ru/C. To prepare the homemade Ru/C catalyst, 80 mg of carbon black (Vulcan XC-72R) was added into 20 mL of DI water under constant stirring and ultrasonic dispersion for 30 min.[3] Then 41 mg of $RuCl_3$ was added into the dispersion while maintaining continuous mixing. After 2 h of stirring, 0.5 g of $NaBH_4$ dissolved in 10 mL of deionized water was added dropwise, and the reaction was allowed to proceed for 12 h. The black powder was then recovered by sedimentation, centrifugation, washing and drying.

Preparation of the working electrode. Prior to electrochemical testing, Pd@Ru octahedra and Pd@Ru icosahedra were loaded onto carbon support (20 wt%). Then Pd@Ru octahedra/C and Pd@Ru icosahedra/C catalysts were dispersed in a mixture of ethanol and 5 wt.% Nation solution. Then, 12 μL (containing 2 μg of Ru) of catalyst ink was dropped onto a glassy carbon electrode (0.196 cm^2).

Electrochemical measurements. All electrochemical tests were conducted using a three-electrode system with a CHI660e electrochemical workstation (Chenhua Instrument, China). A rotation carbon electrode (RDE, diameter: 5 mm) was used as the working electrode, the reference electrode was a Hg/HgO (1 M NaOH) electrode, and the counter electrode was a carbon rod. The potential at zero current density was considered the thermodynamic potential for the reversible hydrogen electrode (RHE). The potentials relative to RHE were calculated using the following equation:

$$E\ (V_{RHE}) = E\ (Hg/HgO) + 0.098\ V + 0.0591 * pH - iR$$

where R is the solution resistance determined by electrochemical impedance spectroscopy (EIS).

The HOR electrochemical measurements were conducted in a H_2-purged 0.1 M KOH aqueous solution. After saturating the electrolyte with pure hydrogen for at least 10 min, the

HOR polarization curves were recorded by sweeping the potential from -0.08 V to 0.9 V (vs RHE) at a scan rate of 1 mV s^{-1} under different rotation rates (400, 900, 1600 and 2500 rpm). The stability test was performed at 0.3 V (vs RHE) for 4000 s. Electrochemical impedance spectra (EIS) were recorded over the frequency range from 100 kHz to 0.1 Hz with an amplitude of applied voltage of 5 mV. The cyclic voltammetry (CV) curves were obtained in a N_2-saturated 0.1 M KOH solution by scanning the potential from 0 V to 1.2 V (vs RHE) at a scan rate of 100 mV s^{-1}. The electrochemically active surface areas (ECSAs) were determined from CO stripping experiments. In these, the rotating disk electrode (RDE) was held at 0.1 V (vs RHE) for 20 min in CO-purged solution to adsorb CO. Then RDE was quickly transferred to a flesh N_2-purged 0.1 M KOH solution, and two CV cycles were recorded in the potential region from 0 V to 1.2 V (vs RHE) at a sweep rate of 20 mV s^{-1}.

The kinetic current density (j_k) was calculated using the Koutecky-Levich equation,

$$\frac{1}{j} = \frac{1}{j_k} + \frac{1}{j_d} = \frac{1}{j_k} + \frac{1}{\beta c_0 \omega^{1/2}}$$

Where j, j_d, β, c_0 and ω represent the current density, diffusion-limited current, Levich constant, solubility of H_2 in alkaline solution and rotation speed, respectively.

The exchange current density (j_0) was calculated by two methods. One is from the Butler-Volmer equation,

$$j_k = j_0\left(e^{\frac{\alpha F}{RT}\eta} - e^{\frac{-(1-\alpha)F}{RT}\eta}\right)$$

Where α, F and R refer to the charge transfer coefficient, Faraday constant and the universal gas constant (8.314 J mol^{-1} K^{-1}), respectively. Another is to perform linear fitting in micro-polarization regions via the Butler-Volmer equation,

$$j_0 = \frac{jRT}{\eta F}$$

The mass activity ($j_{k,m}$) was normalized using the active mass of Ru drop-casted onto the RDE surface, calculated as:

$$MA = \frac{j_k}{m}$$

The specific activity ($j_{0,ECSA}$) was normalized based on the ECSA, calculated as:

$$j_{0,s} = \frac{j_0}{\mathrm{ECSA}}$$

Electrochemical Raman measurement. In situ Raman spectra were acquired using a confocal Raman microscope (WITec Alpha 300R). The excitation source was a 633 nm laser with a power of 10 mW and grating of 600 grooves/mm, while a 50× objective (Zeiss LD EC Epiplan-Neofluar Dic) was used. Each spectrum was recorded with an acquisition time of 120 s and 1 times of accumulation. The electrochemical reactor for in situ Raman measurements was a single cell purchased from Tianjin Aida Hengsheng Technology Development Co., Ltd. The Pd@Ru octahedra/C or Pd@Ru icosahedra/C were loaded onto the glass carbon electrode, with a Pt wire serving as the counter electrode and Ag/AgCl electrode as the reference electrode. Before the measurements, the 0.1 M KOH electrolyte was saturated with H_2 gas, and in situ Raman spectra were collected at varying potentials using a chronoamperometry test.

In situ attenuated total reflection surface-enhanced infrared absorption spectroscopy (ATR-SEIRAS) measurements. In situ ATR-SEIRAS was carried out using Thermo Scientific Nicolet iS50 FTI spectrometer with internal reflection configuration at room temperature. An Au film was first deposited on a smooth surface of a Si prism. The airbrush method was used to completely cover the Au film by the Pd@Ru octahedra/C or Pd@Ru icosahedra/C catalyst. H_2-saturated 0.1 M KOH was used in the measurements. All spectra were collected in absorbance at a resolution of 7.71 cm^{-1}. The background spectrum was collected before each test to correct the data. The measured potential range was from 0.3 to 0 V versus RHE with a potential gap of 0.02 V.

Derivation of Equations for calculating the atomic ratio. The equations to calculate the Pd:Ru atomic ratio in the core-shell icosahedra and octahedra are derived as a function of particle size and thickness of shell.

For Pd@Ru core-shell icosahedra:

Since the Pd seed is an icosahedra, the side length of the surface triangle is defined as **a**, and the distance from the body center to the apex is denoted as **a + 0.22*2n** (where **n** refers to the number of layers). The size of icosahedral particles is measured between two opposite apexes, which is twice the distance from the body center to the vertex (i.e. diameter of the circumscribed sphere), it was $\frac{\sqrt{10+2\sqrt{5}}}{2}a$. Surface Ru has a uniform distribution because of layer-by-layer deposition.

Average size of Pd seed is 15.30 nm.

Volume of core: $V_{core} = \frac{(15+5\sqrt{5})}{12} \times a^3$;

Surface triangle with a side length of Pd seed: $15.30 = \frac{\sqrt{10+2\sqrt{5}}}{4} \times a_1 \times 2$, $a_1 = 8.044$ nm;

Surface triangle with a side length of Pd@Ru icosahedron: $15.30 + 0.22*10 = \frac{\sqrt{10+2\sqrt{5}}}{4} a_2 \times 2$, $a_2 = 9.200$ nm;

Volume of Pd seed: $V_{Pd\ seed} = \frac{15+5\sqrt{5}}{12} \times 8.044^3 = 1135.427\ nm^3$;

Volume of Pd@Ru icosahedron: $V_{ic\text{-}Ru} = \frac{15+5\sqrt{5}}{12} \times 9.200^3 = 1699.023\ nm^3$;

Volume of Ru shell: $V_{Ru\ shell} = V_{ic\text{-}Ru} - V_{Pd\ seed} = 563.596\ nm^3$;

Volume of Pd single atom: $V_{Pd\ single\ atom} = \frac{4}{3}\pi \times 0.137^3 = 0.010770858\ nm^3$;

Volume of Ru single atom: $V_{Ru\ single\ atom} = \frac{4}{3}\pi \times 0.134^3 = 0.010078664\ nm^3$;

Number of Pd atom: $V_{Pd\ seed} / V_{Pd\ single\ atom} = 105416.613$;

Number of Ru atom: $V_{Ru\ shell} / V_{Ru\ single\ atom} = 55919.655$;

So Pd@Ru icosahedron atomic ratio: Pd:Ru = **1.885**, mass ratio: Pd:Ru = 1.985.

For Pd@Ru core-shell octahedra:

The Pd seed is octahedra, so the side length of the surface triangle is noted as **b**. The size of octahedra particles was measured between two opposite apexes, which is the diameter of the circumscribed sphere, it was $\frac{\sqrt{2}}{2}b$.

Average size of Pd seed is 14.60 nm.

Volume of core: $V_{\text{core}} = \frac{\sqrt{2}}{3} \times b^3$;

Surface triangle with a side length of Pd seed: $14.60 = \frac{\sqrt{2}}{2} b_1 \times 2$, $b_1 = 10.324$ nm;

Surface triangle with a side length of Pd@Ru octahedra: $14.60 + 0.22 \times 10 = \frac{\sqrt{2}}{2} b_2 \times 2$, $b_2 = 11.879$ nm;

Volume of Pd seed: $V_{\text{Pd seed}} = \frac{\sqrt{2}}{3} \times 10.324^3 = 518.689$ nm^3;

Volume of Pd@Ru octahedra: $V_{\text{oc-Ru}} = \frac{\sqrt{2}}{3} \times 11.880^3 = 790.272$ nm^3;

Volume of Ru shell: $V_{\text{Ru shell}} = V_{\text{oc-Ru}} - V_{\text{Pd seed}} = 271.583$ nm^3;

Volume of Pd single atom: $V_{\text{Pd single atom}} = \frac{4}{3}\pi \times 0.137^3 = 0.010770858$ nm^3;

Volume of Ru single atom: $V_{\text{Ru single atom}} = \frac{4}{3}\pi \times 0.134^3 = 0.010078664$ nm^3;

Number of Pd atom: $V_{\text{Pd seed}} / V_{\text{Pd single atom}} = 48156.733$;

Number of Ru atom: $V_{\text{Ru shell}} / V_{\text{Ru single atom}} = 26946.294$;

So Pd@Ru octahedra atomic ratio: Pd:Ru = **1.787**, mass ratio: Pd:Ru = 1.882.

Calculation of the lattice expansion. The lattice expansion of Ru shell, $\Delta_{(Ru)}$, was calculated according to the following equation[4]:

$$\Delta_{(Ru)} = \frac{d_{(Ru-shell)} - d_{Ru}}{d_{Ru}} \times 100\%$$

Where $d_{(Ru\text{-}shell)}$ indicates the average Ru-Ru distance of the Ru shell measured by HAADF-STEM, and d_{Ru} is the corresponding bulk value (2.33 Å). For Pd@Ru octahedra, $d_{(Ru\text{-}shell)}$ was measured to be 2.333 Å and the corresponding d_{Ru} is 2.33 Å, thus the $\Delta_{(Ru)}$ was calculated to be 0.1%. For Pd@Ru icosahedra, $d_{(Ru\text{-}shell)}$ was measured to be 2.39 Å and the corresponding d_{Ru} is 2.33 Å. Therefore, the $\Delta_{(Ru)}$ was therefore calculated to be 2.5%.

Density functional theory (DFT) calculations. All DFT calculations were performed using the VASP software, which employs a plane-wave basis set combined with the projector-augmented wave (PAW) method for treating core electrons.[5-8] The calculations incorporated the Perdew, Burke, and Ernzerhof exchange-correlation functional within the generalized gradient approximation (GGA-PBE).[7] Moreover, due to its superior performance in depicting long-range van der Waals interactions, the vdW correction proposed by Grimme (DFT-D3) was adopted.[9] A convergence cutoff of 450 eV was set in the whole calculation for the expansion of wavefunctions over the plane-wave basis set.

The Pd@Ru icosahedra (a = b = 8.099 Å) and Pd@Ru octahedra (a = b = 8.305 Å) were constructed using 3*3*4 unit cells based on the tensile strain determined from HRTEM. All models were constructed with 15 Å of vacuum space. The reciprocal space was sampled by the Γ-centered Monkhorst-Pack scheme using a 3×3×1 K-point grid. The bottom two layers were fixed, and the others were relaxed. Both models were fully relaxed prior to the calculations. The convergence criteria for the electronic self-consistent (SC)-loop were set to 1×10^{-5} eV, and the relaxation was stopped when the total energy change between two ionic steps was smaller than 0.05 eV/Å.

The d-band center (ε_d) is calculated from the atom projected density of states of a single surface metal atom by integrating the states from the bottom of the d band to the Fermi level and referenced to the Fermi energy and is calculated according to the following equation:

$$\varepsilon_d = \int_0^{-\infty} nd(\varepsilon)\varepsilon d\varepsilon \Big/ \int_0^{-\infty} nd(\varepsilon) d\varepsilon$$

Where $nd(\varepsilon)$ is the density of states of d band at a given energy ε.

Besides, the Climbing-Image Nudged Elastic Band (CINEB) method was employed to compare the activation barrier for transition states (TS). The adsorption energy (ΔE_{ad}) of intermediates was calculated as the following equation:

$$\Delta E_{ad} = \Delta E_{ads+surf} - \Delta E_{ads} - \Delta E_{surf}$$

$\Delta E_{ads+surf}$, ΔE_{ads}, and ΔE_{surf} are the energy of the surface with adsorbate, single adsorbate, and surface, respectively.

The Gibbs free energy of HOR elemental steps was calculated as follows:

$$\Delta G = \Delta E + \Delta ZPE - T\Delta S$$

ΔZPE and ΔS represent the zero point energy correction and entropy change, respectively.

Supplementary Figures

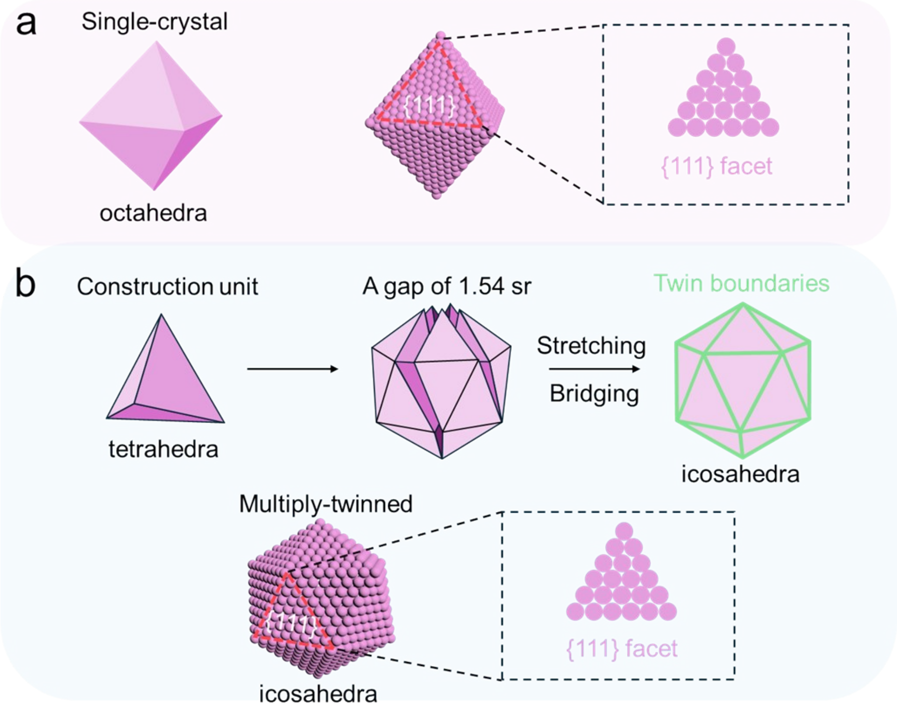

Fig. S1. Schematic illustration showing the characteristics of octahedra and icosahedra.

Note: The icosahedron is a typical structure that has intrinsic strain due to the unique five-fold symmetry, whereas the octahedron shows no strain. Specifically, the icosahedron is a multiply-twinned polyhedron enclosed by {111} facets. It can be considered as an assembly of 20 face-centered cubic (fcc)-structured single-crystal apex-sharing tetrahedron with a five-fold symmetry. However, this assembly mode does not fully fill the space. In order to form a space-filling structure, the bond lengths need to be elongated, leading to the intrinsic strain in icosahedron[10-12]. In contrast, the octahedral structure is a single-crystal polyhedron enclosed by {111} facets. And there is no need for bond length adjustment to fill the space.

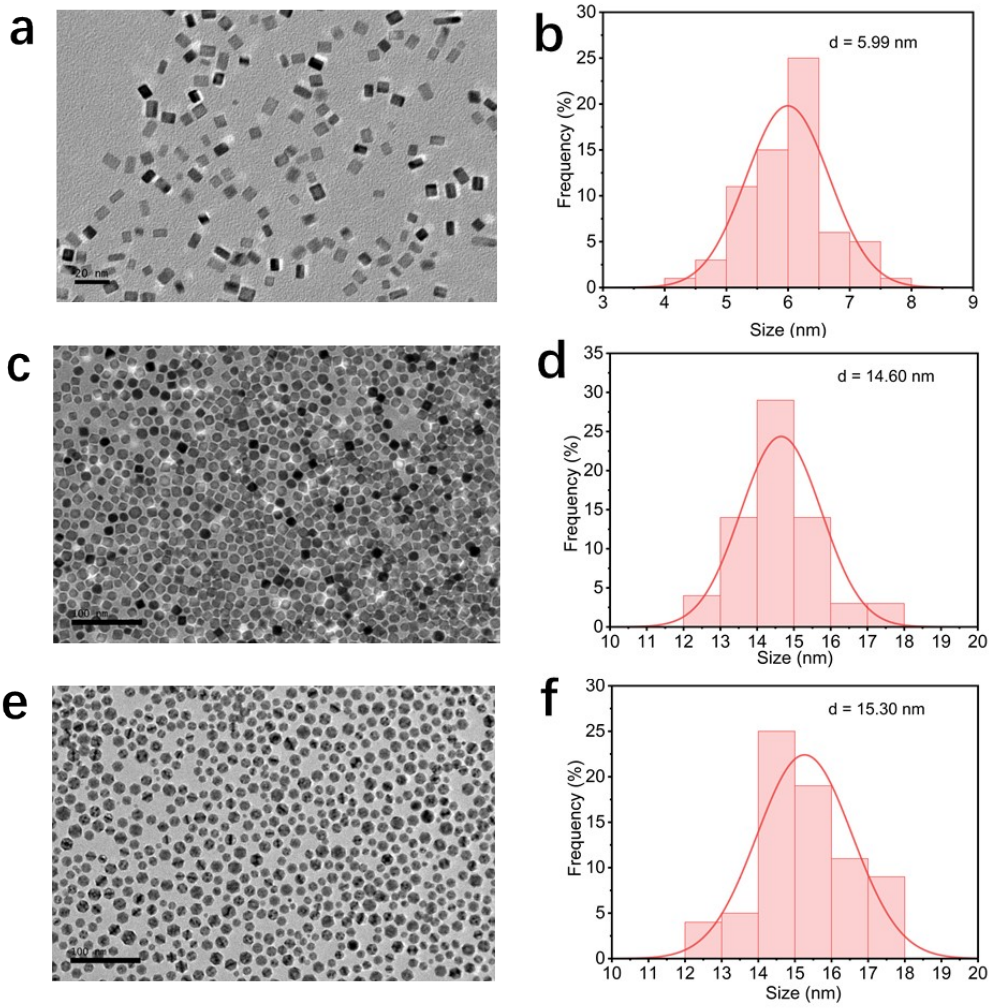

Fig. S2. TEM images and size distribution of Pd cube (a, b), Pd octahedra (c, d) and Pd icosahedra (e, f).

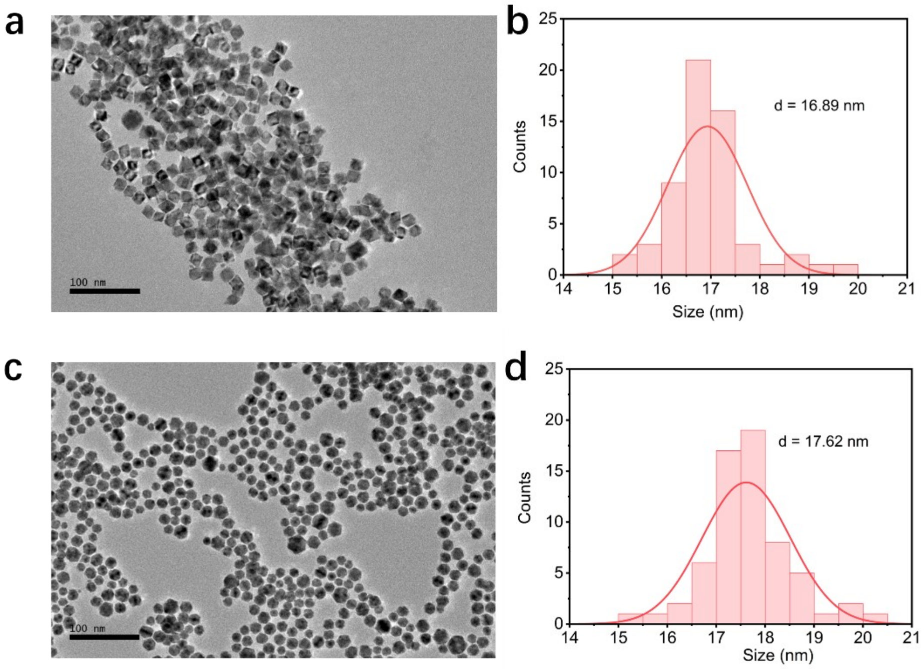

Fig. S3. TEM images and size distribution of Pd@Ru octahedra (a, b), Pd@Ru icosahedra (c, d).

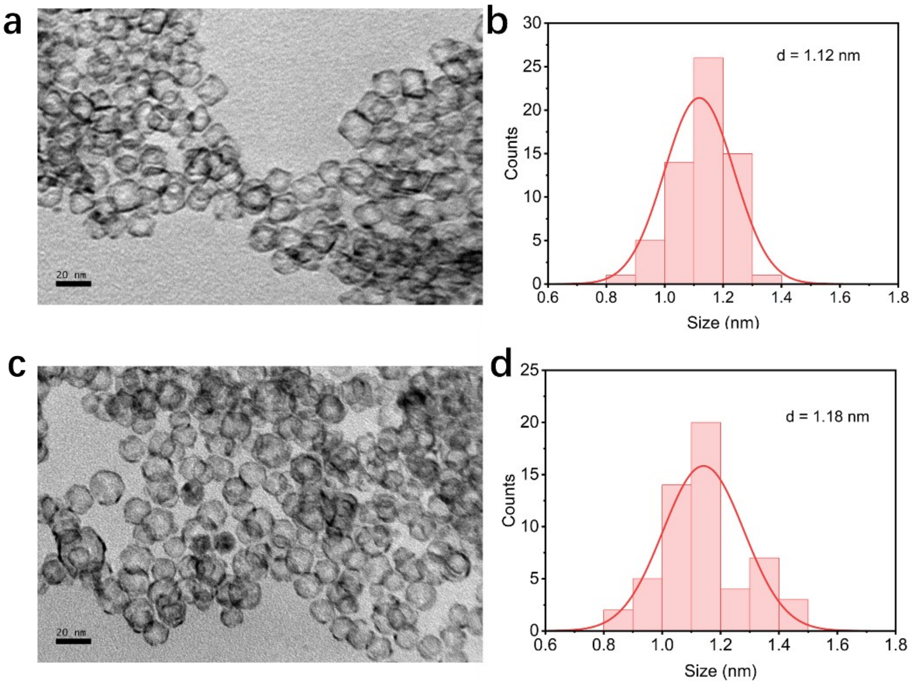

Fig. S4. TEM images and thickness distribution of Ru shell of Pd@Ru octahedra (a, b) and Pd@Ru icosahedra (c,d).

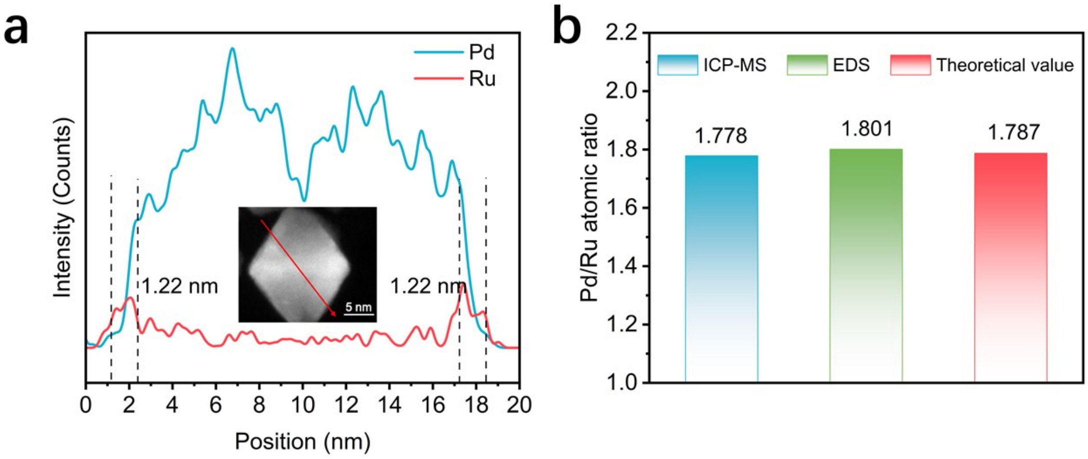

Fig. S5. (a) EDS line scanning profiles across the red arrows shown in the inset image of Pd@Ru octahedra. (b) Elements content comparison of Pd and Ru. Data from ICP-MS and EDS.

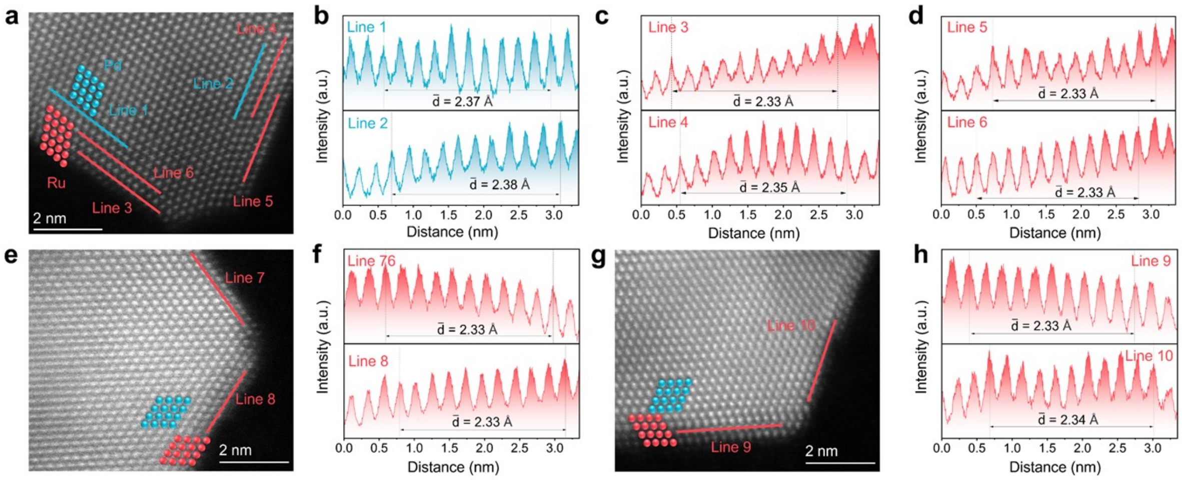

Fig. S6. (a) Atomically resolved HAADF-STEM image of Pd@Ru octahedra. (b) The intensity profiles are taken along the blue lines in (a). (c,d) The intensity profiles are taken along the red lines in (a). (e,g) Atomically resolved HAADF-STEM image of Pd@Ru octahedra. (f, h) The intensity profiles are taken along the red lines in (e,g), respectively.

Note: Eight additional positions from different particles in the electron microscopy images were analyzed. The measured Ru-Ru distances were 2.33 Å, 2.34 Å and 2.35 Å, respectively. Averaging these all nine measurements (Fig. 1f, Fig. S6), the average surface strain of Ru surface on Pd octahedron is only 0.1%, which is virtually negligible.

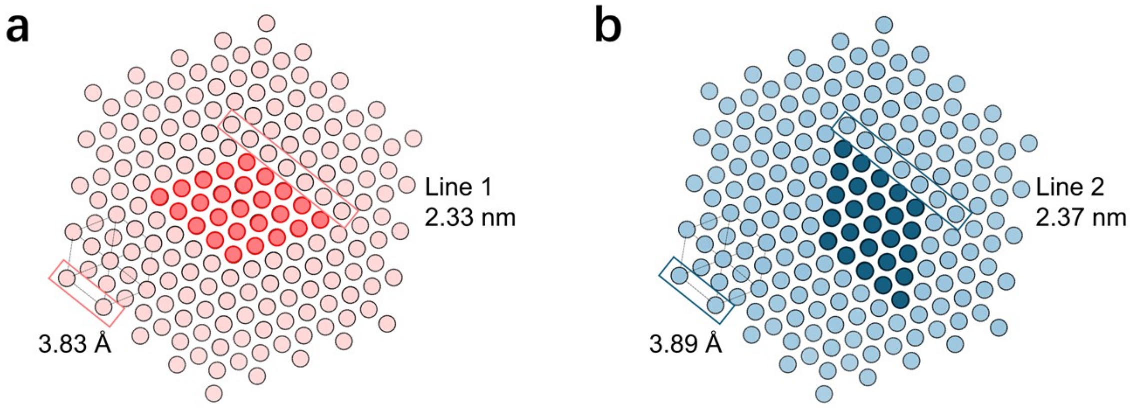

Fig. S7. The model structure of Ru (a) and Pd (b) in Pd@Ru octahedra according to the images from HAADF-STEM, showing the {111} planes parallel to the plane of paper.

Note: The arrangement in Pd@Ru icosahedra is similar to that of Pd@Ru octahedra, both of which exhibit the {111} plane as the projection, although there are slight differences in the atomic distances: 2.39 nm for Ru-Ru (Line 1) and 2.43 nm for Pd-Pd (Line 2).

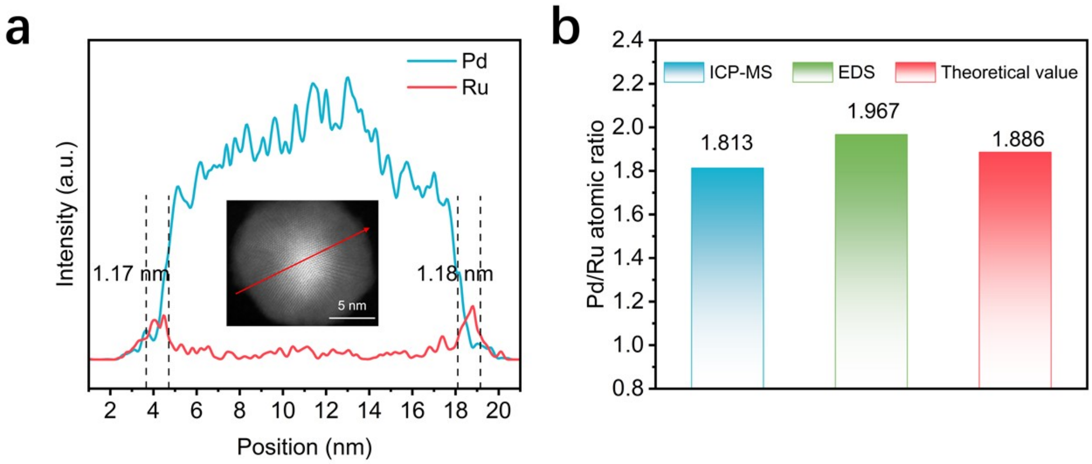

Fig. S8. (a) EDS line scanning profiles across the red arrows shown in the inset image of Pd@Ru icosahedra. (b) Elements content comparison of Pd and Ru. Data from ICP-MS and EDS.

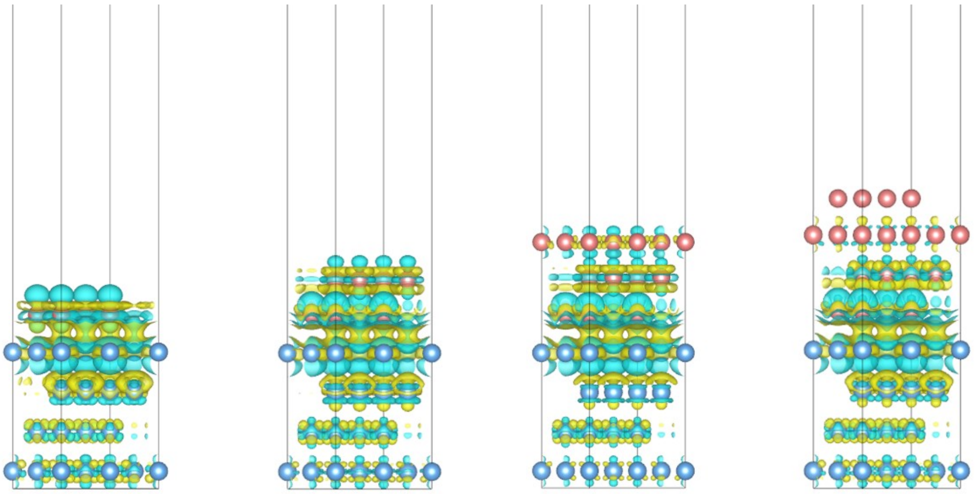

Fig. S9. Difference charge density of Pd@Ru slabs with different layers of Ru ranging from one to four.

Note: The slabs for difference charge density calculation were built by putting Pd (111) slabs at the bottom, noted as Pd@Ru slabs. However, Pd atoms will not be taken into account in the calculations for the subsequent four layers of Ru atoms in order to simplify the calculations, because the electrons of Pd will not have an impact on the catalytic reaction of surface Ru atoms.

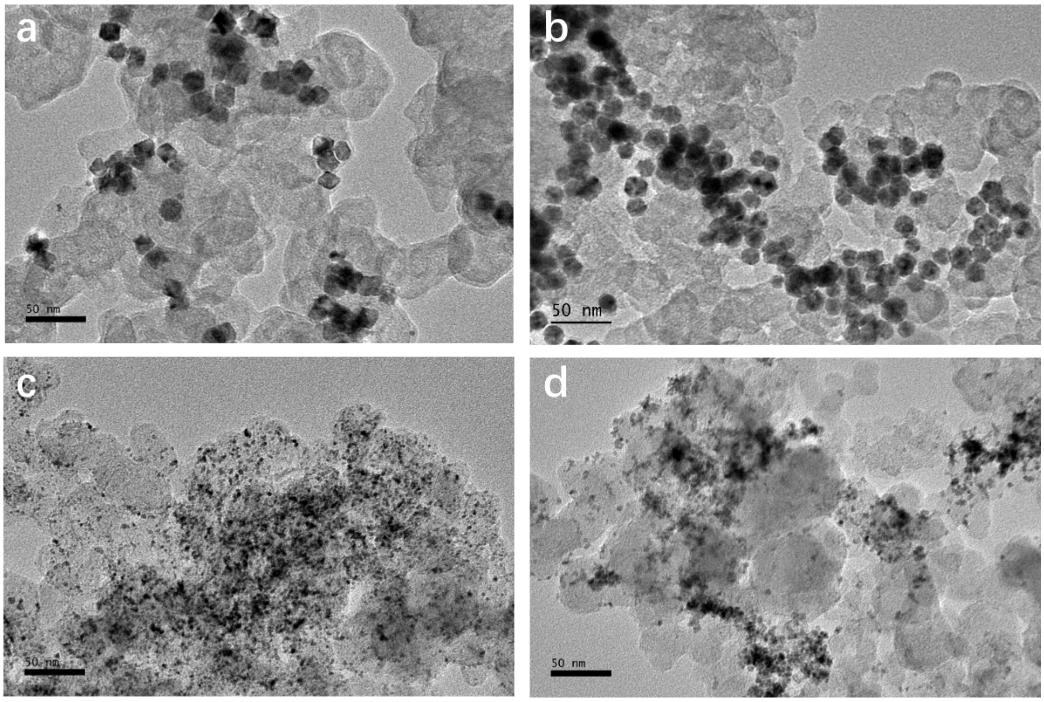

Fig. S10. TEM images of Pd@Ru octahedra/C (a), Pd@Ru icosahedra/C (b), commercial Pt/C (c) and homemade Ru/C (d).

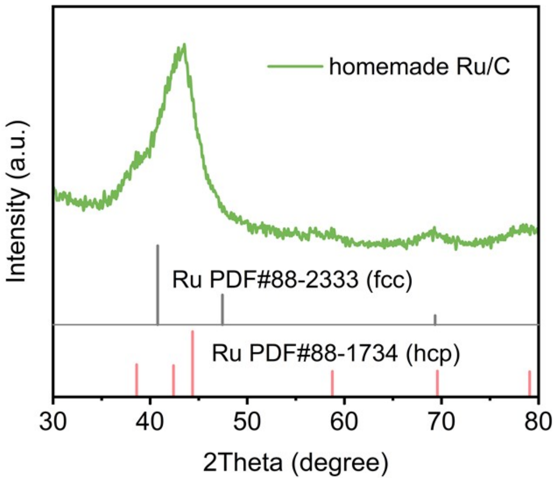

Fig. S11. XRD patterns of the homemade Ru/C catalyst.

Note: The XRD pattern shows that all the peaks can be indexed to the standard hexagonal close-packed (hcp) Ru phase (PDF#88-1734), confirming that the Ru in the catalyst adopts the hcp structure.

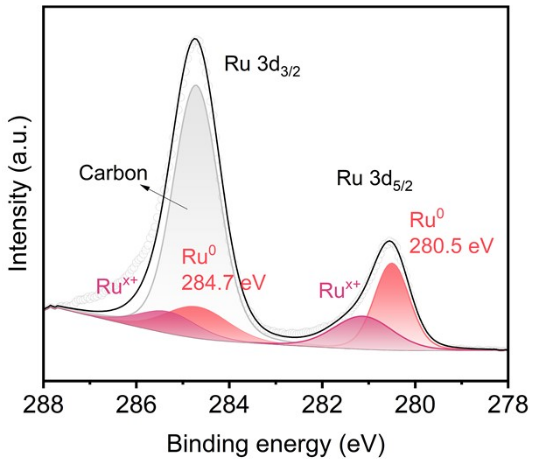

Fig. S12. High-resolution XPS spectra of Ru 3d in the homemade Ru/C catalyst.

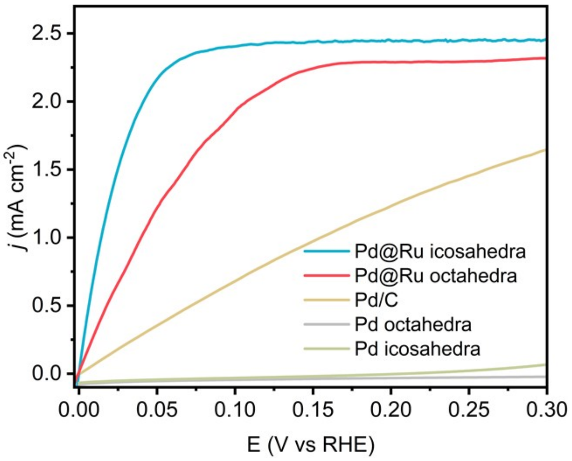

Fig. S13. HOR polarization curves for Pd icosahedra, Pd octahedra, Pd/C, Pd@Ru icosahedra and Pd@Ru octahedra.

Note: The polarization curves were obtained in H_2-saturated 0.1 M KOH solution at a rotating speed of 1600 rpm. Pd icosahedral seeds and Pd octahedral seeds both show negligible HOR activity, which strongly suggests that the enhanced catalytic activity of Pd@Ru derived from the Ru layers.

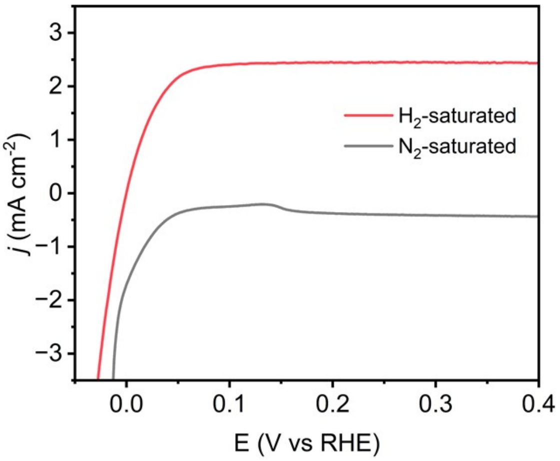

Fig. S14. Polarization curves on Pd@Ru icosahedra/C in N_2-saturated and H_2-saturated 0.1 M KOH solution.

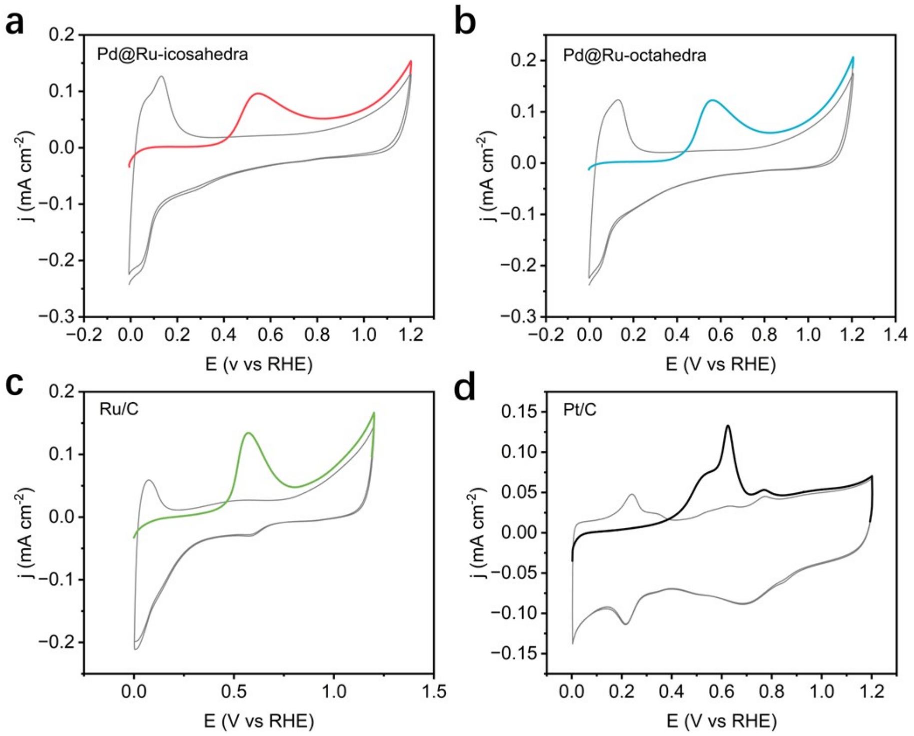

Fig. S15. The cyclic voltammetry (CV) curves of Pd@Ru icosahedra/C (a), Pd@Ru octahedra/C (b), Ru/C (c) and Pt/C (d) as well as the corresponding CO-stripping, respectively.

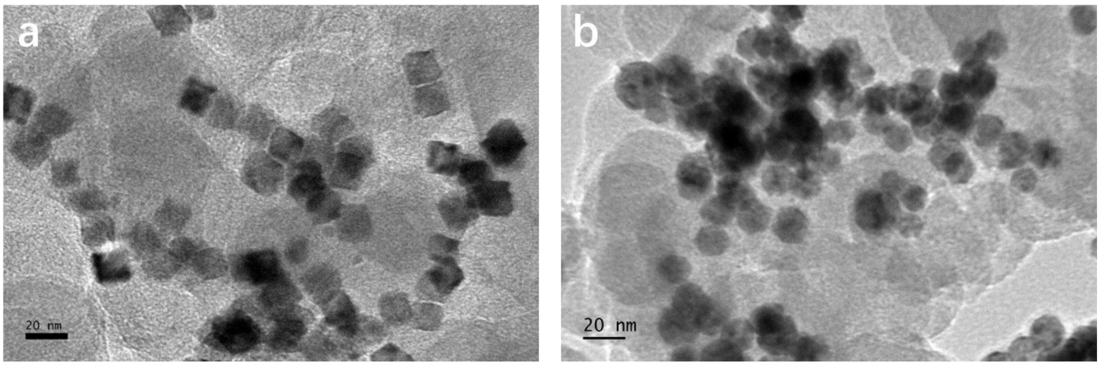

Fig. S16. TEM images of Pd@Ru octahedra/C (a) and Pd@Ru icosahedra/C (b) after durability tests.

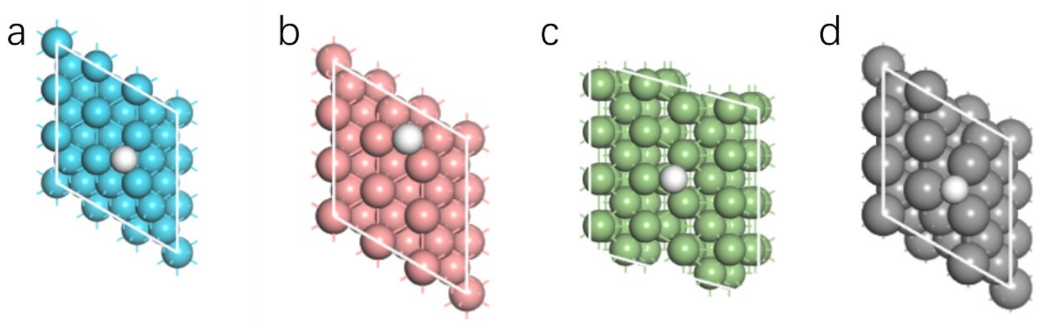

Fig. S17. Theoretical model structures of H* on Pd@Ru icosahedra (a), Pd@Ru octahedra (b), hcp-Ru(101) (c) and fcc-Pt(111) (d).

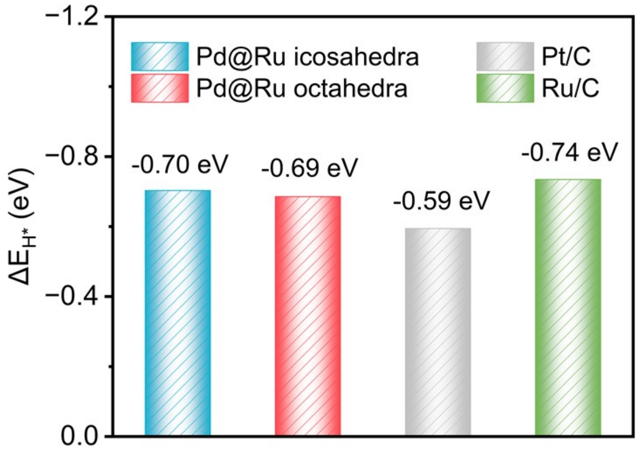

Fig. S18. The adsorption energy of H* on Pd@Ru icosahedra, Pd@Ru octahedra, commercial Pt/C and Ru/C catalysts.

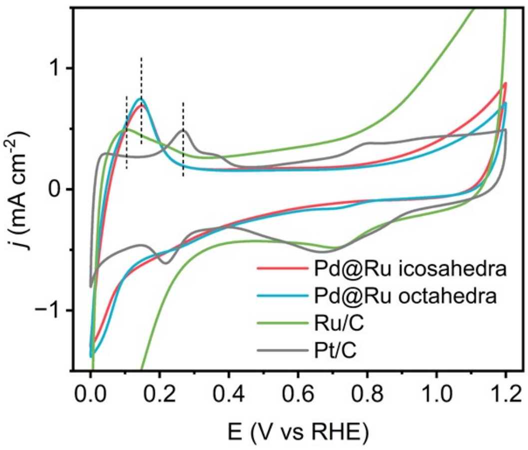

Fig. S19. CV curves of the different electrocatalysts in N_2-saturated 0.1 M KOH solution. Similar HBE values were also identified by similar positions of CV peaks experimentally.

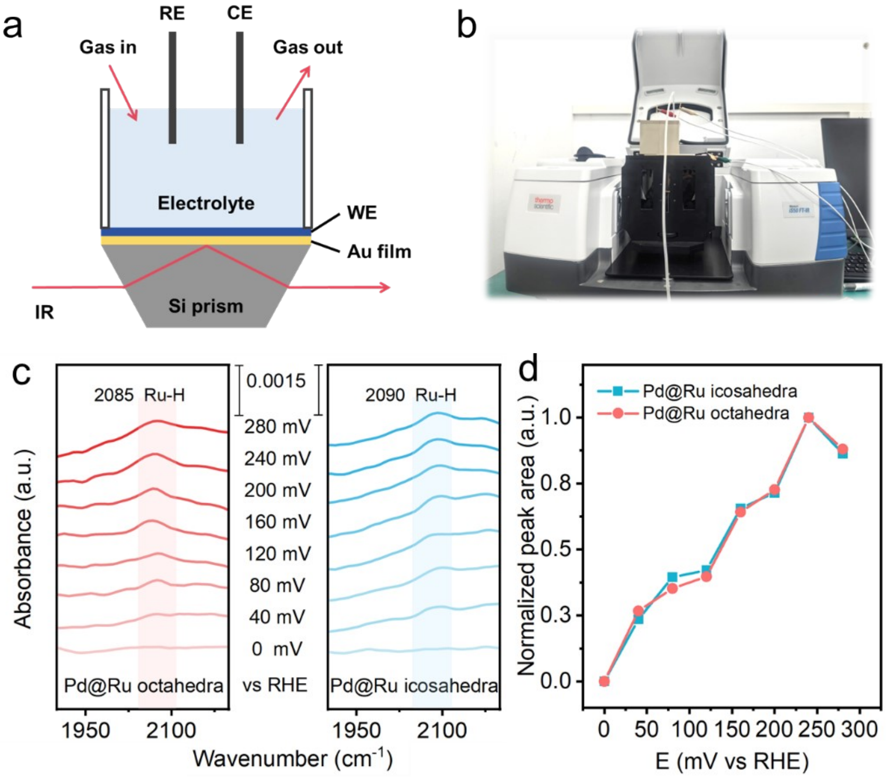

Fig. S20. In situ ATR-SEIRAS analysis of Pd@Ru octahedra and Pd@Ru icosahedra. (a) Schematic representation of the in situ ATR-SEIRAS setup. (b) The photo of the in situ ATR-SEIRAS testing device. (c) In situ ATR-SEIRAS spectra of Pd@Ru icosahedra and Pd@Ru octahedra collected at different applied potentials in H_2-saturated 0.1 M KOH. d) Normalized Ru-H peak area with potentials on the basis of the data in (c).

Note: In the in situ ATR-SEIRAS spectra, both Pd@Ru octahedra and Pd@Ru icosahedra exhibit similar Ru-hydrogen vibrations in the range of 2000-2130 cm^{-1} [13-14]. The peak intensity of Ru-H for Pd@Ru octahedra is comparable to that of Pd@Ru icosahedra at nearly all potentials, suggesting a minimal difference in their proton accumulation. Additionally, the Ru-H band for Pd@Ru octahedra is located at ~2085 cm^{-1}, which is close to the Ru-H band at around 2090 cm^{-1} for Pd@Ru icosahedra, implying that their Ru-H bonding strengths are similar. Together with the in situ ATR-SEIRAS and calculation results, these findings indicate that the performance difference driven by the introduced strain effect between the two catalysts cannot be attributed to H* accumulation.

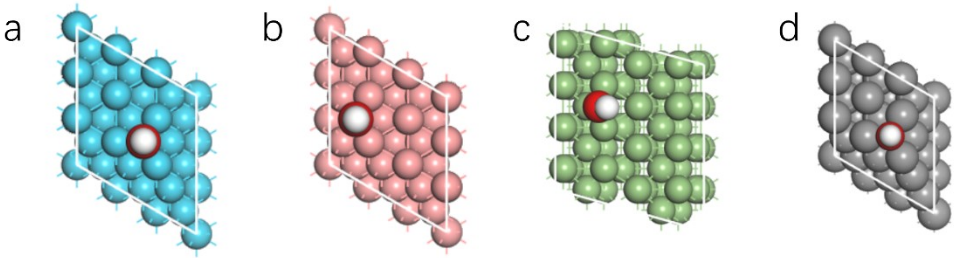

Fig. S21. The optimal theoretical model structure of OH* on Pd@Ru icosahedra (a), Pd@Ru octahedra (b), hcp-Ru(101) (c) and fcc-Pt(111) (d).

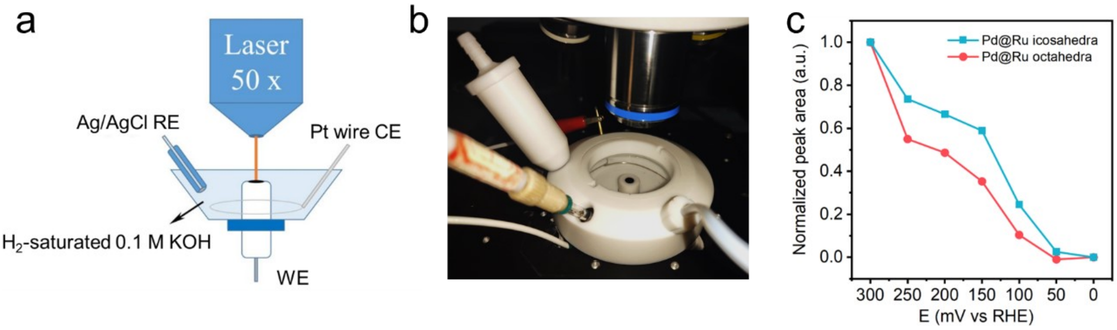

Fig. S22. In situ Raman analysis of Pd@Ru octahedra and Pd@Ru icosahedra. (a) Schematic illustration of the in situ Raman spectroscopy setup. (b) The photo of our in situ Raman testing device. (c) Normalized Raman intensity of OH_{ad} bands with potentials on the basis of the Raman data in Fig. 4d.

Note: An intensified Ru-*OH adsorption peak was detected at 795 cm^{-1} for Pd@Ru icosahedra[15-16]. In contrast, a weaker Ru-*OH binding was probed at 802 cm^{-1} for Pd@Ru octahedra, confirming the weakened OH* binding strengths (OHBE). Such spectroscopy outcomes agree well with our DFT calculations, both of which are supportive of our mechanistic proposals.

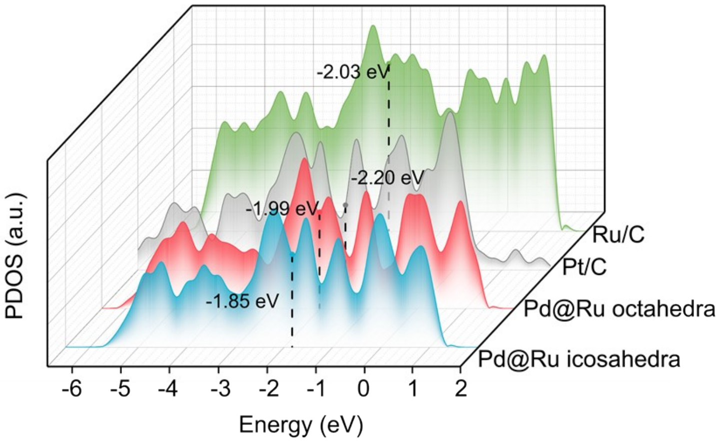

Fig. S23. Calculated projected density of state (PDOS) of Ru sites in Pd@Ru icosahedra, Pd@Ru octahedra, Pt/C and Ru/C. The vertical grey lines denote d-band centers.

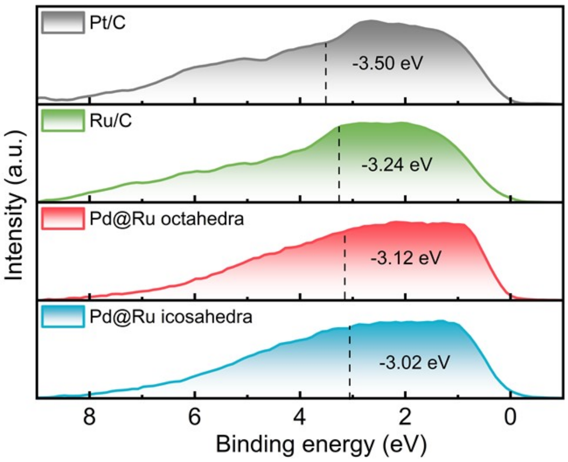

Fig. S24. XPS valence band spectra recorded from Pd@Ru icosahedra, Pd@Ru octahedra, Ru/C and Pt/C, respectively. The d-band centers are marked with white lines.

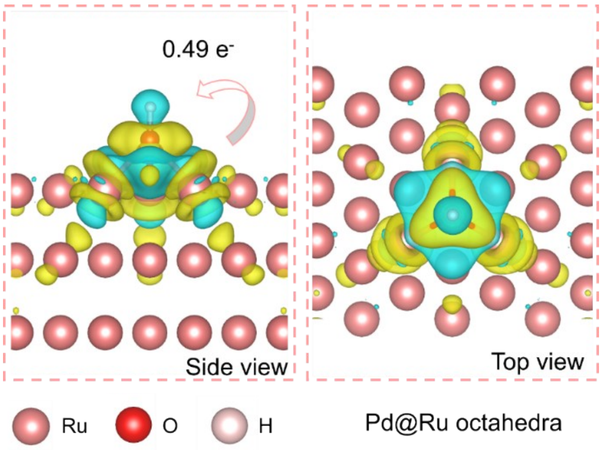

Fig. S25. Side and top view of electronic difference and Bader analysis for Pd@Ru octahedra. Yellow and blue counters represent the isosurfaces of electronic charge accumulation.

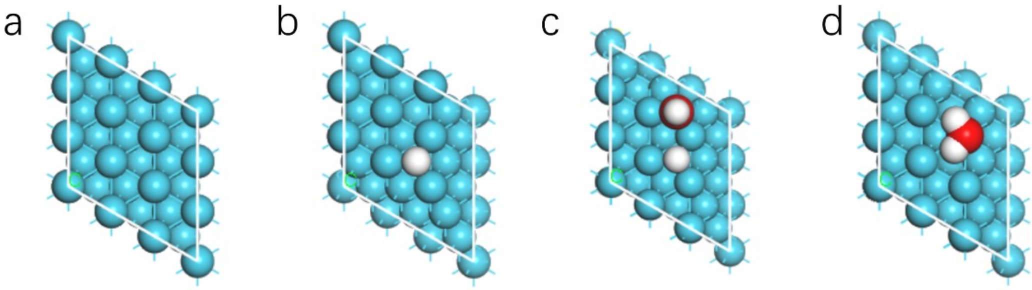

Fig. S26. The optimal theoretical model structure of pristine Pd@Ru icosahedra (a) and H* (b), H*+OH* (c), H_2O* (d) intermediates absorbed on Pd@Ru icosahedra during alkaline HOR process.

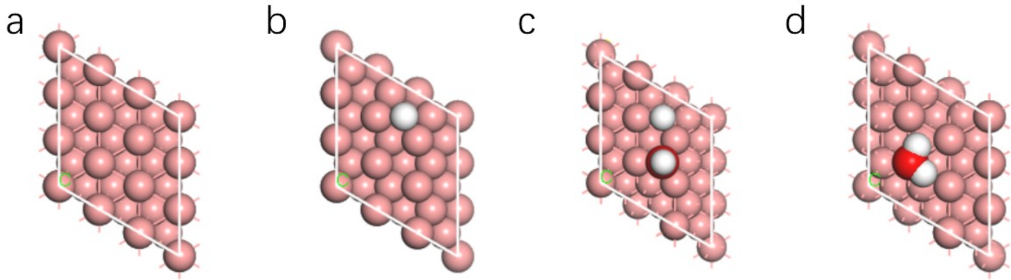

Fig. S27. Stable configurations of pristine Pd@Ru octahedra (a) and H* (b), H*+OH* (c), H_2O* (d) intermediates absorbed on Pd@Ru octahedra during alkaline HOR process.

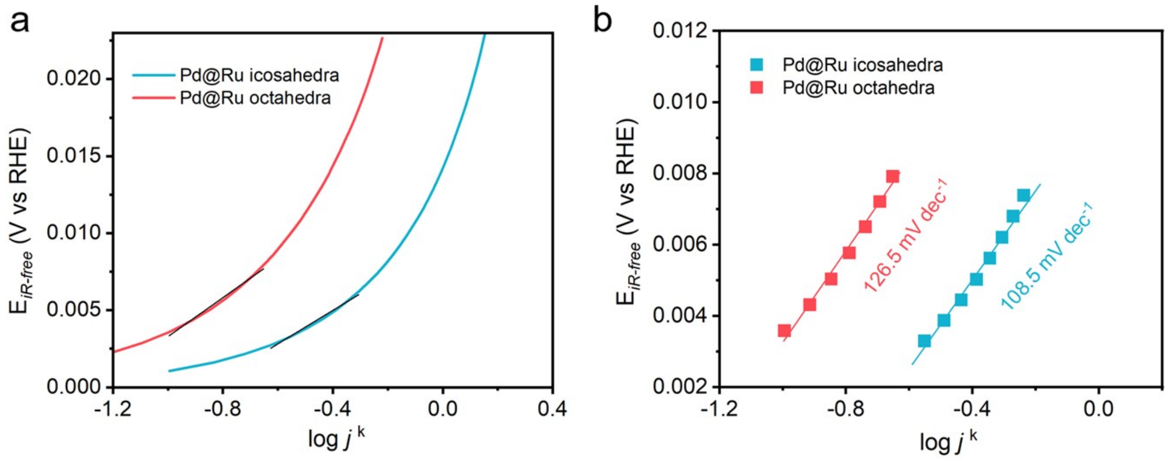

Fig. S28. (a) Tafel plots of HOR branch, (b) Tafel slopes of HOR for Pd@Ru icosahedra and Pd@Ru octahedra in H_2-saturated 0.1 M KOH solution.

Note: In order to precisely identify the RDS of HOR, the Tafel slope (TS) determined from the polarization curve is generally used as a descriptor. In our system, the Tafel plots of alkaline HOR branches are depicted in Fig. S28. The Tafel slops of Pd@Ru icosahedra and Pd@Ru octahedra are calculated to be 108.5 mV dec^{-1} and 126.5 mV dec^{-1}, respectively. For the Volmer-Tafel mechanism with Volmer being the RDS, Tafel slope is approximately to be 118 mV dec-1 at 298 K, demonstrating a symmetric figure in the Butler-Volmer fitting. Based on above fact, it can be determined that the alkaline HOR processes on this two catalysts are undergoes with the Volmer step as the RDS, which constitutes the main energy barrier.

Table S1. ICP-MS and EDS of Pd@Ru octahedra.

	Pd (concentration or fraction)	Ru (concentration or fraction)	Measured Pd/Ru atomic ratio	Ideal Pd/Ru atomic ratio
ICP-MS	22.1 ppb	11.8 ppb	1.778	1.787
EDS	64.3%	35.7%	1.801	1.787

Table S2. ICP-MS and EDS of Pd@Ru icosahedra.

	Pd (concentration or fraction)	**Ru (concentration or fraction)**	**Measured Pd/Ru ratio**	**Ideal Pd/Ru ratio**
ICP-MS	43.9 ppb	23.0 ppb	1.813	1.885
EDS	66.3%	33.7%	1.967	1.885

Table S3. Calculated exchange current density from micro-polarization regions and Tafel regions.

Catalysts	Exchange current density (mA cm^{-2})	
	Micro-polarization regions	**Tafel regions**
Pd@Ru icosahedra/C	2.235	2.326
Pd@Ru octahedra/C	1.259	1.250
Pt/C	0.796	0.842
Ru/C	0.694	0.637

Table S4. Summary of alkaline HOR performance for catalysts studied in this work.

Electrocatalysts	**ECSA (m^2/g)**	**$j_{0,ECSA}$ ($mA\ cm^{-2}$)**	**Loading ($ug_{Ru/Pt}\ cm^{-2}$)**	**$j_{k,m}$ ($A\ mg_{Ru/Pt}^{-1}$)**
Pd@Ru icosahedra/C	53.26	0.41	2	2.52
Pd@Ru octahedra/C	55.29	0.22	2	0.90
Pt/C	57.62	0.14	2	0.49
Ru/C	51.64	0.13	2	0.33

Table S5. Summary of recently reported Ru-based and other electrocatalysts for HOR in 0.1 M KOH.

Electrocatalysts	$j_{k,m}$ (A $mg_{Ru/Rh/Ir}^{-1}$)	$j_{k,m}$ (A mg_{PGM}^{-1})	$j_{0,ECSA}$ (mA $cm^{-2}{}_{Ru}$)	**Reference**
Pd@Ru icosahedra	**2.52**	**0.865**	**0.41**	**This work**
Rh_2Sb NBs/C	3.25	3.25	0.506	17
Ru/Ni-NiO@C	2.79	2.79	0.084	18
Sn-Ru/C	1.79	1.79	0.47	19
$Ru_{0.90}Pt_{0.10}$NTs	1.37	1.24	2.43	20
IrNi@Ir/C	1.12	1.12	1.22	21
Ru@Pt NPs	1.03	-	-	22
hcp/fcc-Ru	1.016	1.016	0.664	23
Ru_3Sn_7/C	0.658	0.658	0.263	24
Ru Colloidosome	0.46	0.46	0.045	25
Ru-Ir-C	0.22	-	0.28	26
Ru/CeO_2/C	8.06	8.06	2.85	27
P-Ru/C	-	-	0.72	28
Ir_1Ru_1 NWs/C	1.416	1.416	0.126	29
IO-Ru-TiO_2/C	0.907	0.907	1.13	30
$RuNi_1$	2.7	2.7	-	31
RhMo NSs	6.96	6.96	-	32
Ni/NiO/C-700	0.005	0.005	0.026	33
Ru@TiO_2	0.29	0.29	-	34
PtNb/NbO_x-C	0.36	0.36	0.8	35
PdCu/C-500	0.522	0.522	0.883	36
$Ru_{0.95}Co_{0.05}$/C	0.16	0.16	0.14	37
PtRu NWs	-	0.6	-	38
IrNi@PtIr	-	0.854	1.656	39
Ru@Ir/C	-	0.816	0.792	40

Reference

1 Zhao, M.; Figueroa-Cosme, L.; Elnabawy, A. O.; Vara, M.; Yang, X.; Roling, L. T.; Chi, M.; Mavrikakis, M.; Xia, Y., Synthesis and Characterization of Ru Cubic Nanocages with a Face-Centered Cubic Structure by Templating with Pd Nanocubes, *Nano Lett.,* 2016, **16**, 5310-5317.

2 Zhao, M.; Elnabawy, A. O.; Vara, M.; Xu, L.; Hood, Z. D.; Yang, X.; Gilroy, K. D.; Figueroa-Cosme, L.; Chi, M.; Mavrikakis, M.; Xia, Y., Facile Synthesis of Ru-Based Octahedral Nanocages with Ultrathin Walls in a Face-Centered Cubic Structure, *Chem. Mater.,* 2017, **29**, 9227-9237.

3 Yang, Z.; Lai, W.; He, B.; Wang, J.; Yu, F.; Liu, Q.; Liu, M.; Zhang, S.; Ding, W.; Lin, Z.; Huang, H., Tailoring Interfacial Chemistry of Defective Carbon-Supported Ru Catalyst Toward Efficient and CO-Tolerant Alkaline Hydrogen Oxidation Reaction, *Adv. Energy Mater.,* 2023, **13**, 2300881.

4 Liu, G.; Zhou, W.; Ji, Y.; Chen, B.; Fu, G.; Yun, Q.; Chen, S.; Lin, Y.; Yin, P.-F.; Cui, X.; Liu, J.; Meng, F.; Zhang, Q.; Song, L.; Gu, L.; Zhang, H., Hydrogen-Intercalation-Induced Lattice Expansion of Pd@Pt Core-Shell Nanoparticles for Highly Efficient Electrocatalytic Alcohol Oxidation, *J. Am. Chem. Soc.,* 2021, **143**, 11262-11270.

5 Kresse, G.; Hafner, J., Ab Initio Molecular-Dynamics Simulation of the Liquid-Metal-Amorphous-Semiconductor Transition in Germanium, *Phys. Rev. B,* 1994, **49**, 14251-14269.

6. Kresse, G.; Joubert, D., From Ultrasoft Pseudopotentials to the Projector Augmented-Wave Method, *Phys. Rev. B,* 1999, **59**, 1758-1775.

7 Perdew, J. P.; Burke, K.; Ernzerhof, M., Generalized Gradient Approximation Made Simple, *Phys. Rev. Lett.,* 1996, **77**, 3865-3868.

8 Kresse, G.; Furthmüller, J., Efficient Iterative Schemes for Ab Initio Total-Energy Calculations Using a Plane-Wave Basis Set, *Phys. Rev. B,* 1996, **54**, 11169-11186.

9 Grimme, S.; Antony, J.; Ehrlich, S.; Krieg, H., A Consistent and Accurate Ab Initio Parametrization of Density Functional Dispersion Correction (DFT-D) for the 94 Elements H-Pu, *J. Chem. Phys.,* 2010, **132**, 154104.

10 Choi, S. I.; Herron, J. A.; Scaranto, J.; Huang, H.; Wang, Y.; Xia, X.; Lv, T.; Park, J.;

Peng, H. C.; Mavrikakis, M.; Xia, Y., A Comprehensive Study of Formic Acid Oxidation on Palladium Nanocrystals with Different Types of Facets and Twin Defects, *ChemCatChem,* 2015, **7**, 2077-2084.

11 Li , C.; Sato, R.; Kanehara, M.; Zeng, H.; Bando, Y.; Teranishi, T., Controllable Polyol Synthesis of Uniform Palladium Icosahedra: Effect of Twinned Structure on Deformation of Crystalline Lattices, *Angew. Chem. Int. Ed.,* 2009, **48**, 6883-6887.

12 Zhao, J.; Wang, M.; Peng, Y.; Ni, J.; Hu, S.; Zeng, J.; Chen, Q., Exploring the Strain Effect in Single Particle Electrochemistry Using Pd Nanocrystals, *Angew. Chem. Int. Ed.,* 2023, **62**, e202304424.

13 Xue, Y.; Shi, L.; Liu, X.; Fang, J.; Wang, X.; Setzler, B. P.; Zhu, W.; Yan, Y.; Zhuang, Z., A Highly-Active, Stable and Low-Cost Platinum-Free Anode Catalyst Based on RuNi for Hydroxide Exchange Membrane Fuel Cells, *Nat. Commun.,* 2020, **11**, 5651.

14 Wei, L.; Dong, Y.; Yan, W.; Zhang, Y.; Zhan, C.; Huang, W.-H.; Pao, C.-W.; Hu, Z.; Lin, H.; Xu, Y.; Geng, H.; Huang, X., Hollow Pt-Encrusted RuCu Nanocages Optimizing OH Adsorption for Efficient Hydrogen Oxidation Electrocatalysis, *Angew. Chem. Int. Ed.,* 2025, **64**, e202420177.

15 Wang, Y.-H.; Wang, X.-T.; Ze, H.; Zhang, X.-G.; Radjenovic, P. M.; Zhang, Y.-J.; Dong, J.-C.; Tian, Z.-Q.; Li, J.-F., Spectroscopic Verification of Adsorbed Hydroxy Intermediates in the Bifunctional Mechanism of the Hydrogen Oxidation Reaction, *Angew. Chem. Int. Ed.,* 2021, **60**, 5708-5711.

16 Lin, F.; Luo, H.; Li, L.; Lv, F.; Chen, Y.; Zhang, Q.; Han, X.; Wang, D.; Li, M.; Luo, Y.; Wang, K.; Gu, L.; Wang, Q.; Zhao, X.; Luo, M.; Guo, S., Synthesis of Isolated Ru-O_3 Sites on Hexagonal Close-Packed Intermetallic Penta-Metallene for Hydrogen Oxidation Electrocatalysis, *Nat. Synth.,* 2025, **4**, 399-409.

17 Zhang, Y.; Li, G.; Zhao, Z.; Han, L.; Feng, Y.; Liu, S.; Xu, B.; Liao, H.; Lu, G.; Xin, H. L.; Huang, X., Atomically Isolated Rh Sites within Highly Branched Rh_2Sb Nanostructures Enhance Bifunctional Hydrogen Electrocatalysis, *Adv. Mater.,* 2021, **33**, 2105049.

18 Yang, Y.; Huang, Y.; Zhou, S.; Liu, Y.; Shi, L.; Isimjan, T. T.; Yang, X., Delicate Surface Vacancies Engineering of Ru Doped MOF-Derived Ni-NiO@C Hollow Microsphere Superstructure to Achieve Outstanding Hydrogen Oxidation Performance, *J. Energy*

Chem., 2022, **72**, 395-404.

19 Wu, L.; Su, L.; Liang, Q.; Zhang, W.; Men, Y.; Luo, W., Boosting Hydrogen Oxidation Kinetics by Promoting Interfacial Water Adsorption on d-p Hybridized Ru Catalysts, *ACS Catal.,* 2023, **13**, 4127-4133.

20 St. John, S.; Atkinson, R. W., III; Unocic, K. A.; Unocic, R. R.; Zawodzinski, T. A., Jr.; Papandrew, A. B., Platinum and Palladium Overlayers Dramatically Enhance the Activity of Ruthenium Nanotubes for Alkaline Hydrogen Oxidation, *ACS Catal.,* 2015, **5**, 7015-7023.

21 Liu, D.; Lu, S.; Xue, Y.; Guan, Z.; Fang, J.; Zhu, W.; Zhuang, Z., One-Pot Synthesis of IrNi@Ir Core-Shell Nanoparticles as Highly Active Hydrogen Oxidation Reaction Electrocatalyst in Alkaline Electrolyte, *Nano Energy,* 2019, **59**, 26-32.

22 Elbert, K.; Hu, J.; Ma, Z.; Zhang, Y.; Chen, G.; An, W.; Liu, P.; Isaacs, H. S.; Adzic, R. R.; Wang, J. X., Elucidating Hydrogen Oxidation/Evolution Kinetics in Base and Acid by Enhanced Activities at the Optimized Pt Shell Thickness on the Ru Core, *ACS Catal.,* 2015, **5**, 6764-6772.

23 Li, Y.; Yang, C.; Yue, J.; Cong, H.; Luo, W., Polymorphism-Interface-Induced Work Function Regulating on Ru Nanocatalyst for Enhanced Alkaline Hydrogen Oxidation Reaction, *Adv. Funct. Mater.,* 2023, **33**, 2211586.

24 Su, L.; Fan, X.; Jin, Y.; Cong, H.; Luo, W., Hydroxyl-Binding Energy-Induced Kinetic Gap Narrowing between Acidic and Alkaline Hydrogen Oxidation Reaction on Intermetallic Ru_3Sn_7 Catalyst, *Small,* 2023, **19**, 2207603.

25 Yang, X.; Ouyang, B.; Shen, P.; Sun, Y.; Yang, Y.; Gao, Y.; Kan, E.; Li, C.; Xu, K.; Xie, Y., Ru Colloidosome Catalysts for the Hydrogen Oxidation Reaction in Alkaline Media, *J. Am. Chem. Soc.,* 2022, **144**, 11138-11147.

26 Ishikawa, K.; Ohyama, J.; Okubo, K.; Murata, K.; Satsuma, A., Enhancement of Alkaline Hydrogen Oxidation Reaction of Ru-Ir Alloy Nanoparticles through Bifunctional Mechanism on Ru-Ir Pair Site, *ACS Appl. Mater. Interfaces,* 2020, **12**, 22771-22777.

27 Cheng, Z.; Yang, Y.; Yang, J.; Chen, S.; Wang, P.; Wang, P.; Tong, H.; Wang, C.; Chen, Q., Oxygen-Vacancy-Rich CeO_2/Ru Nanoparticles Enable a High-Performance Catalyst for Alkaline Hydrogen Oxidation, *J. Mater. Chem. A,* 2024, **12**, 4240-4248.

28 Zhao, Y.; Wang, X.; Cheng, G.; Luo, W., Phosphorus-Induced Activation of Ruthenium for Boosting Hydrogen Oxidation and Evolution Electrocatalysis, *ACS Catal.,* 2020, **10**, 11751-11757.

29 Qin, B.; Yu, H.; Gao, X.; Yao, D.; Sun, X.; Song, W.; Yi, B.; Shao, Z., Ultrathin IrRu Nanowire Networks with High Performance and Durability for the Hydrogen Oxidation Reaction in Alkaline Anion Exchange Membrane Fuel Cells, *J. Mater. Chem. A,* 2018, **6**, 20374-20382.

30 Jiang, J.; Tao, S.; He, Q.; Wang, J.; Zhou, Y.; Xie, Z.; Ding, W.; Wei, Z., Interphase-Oxidized Ruthenium Metal with Half-Filled d-Orbitals for Hydrogen Oxidation in an Alkaline Solution, *J. Mater. Chem. A,* 2020, **8**, 10168-10174.

31 Mao, J.; He, C.-T.; Pei, J.; Liu, Y.; Li, J.; Chen, W.; He, D.; Wang, D.; Li, Y., Isolated Ni Atoms Dispersed on Ru Nanosheets: High-Performance Electrocatalysts toward Hydrogen Oxidation Reaction, *Nano Lett.,* 2020, **20**, 3442-3448.

32 Zhang, J.; Liu, X.; Ji, Y.; Liu, X.; Su, D.; Zhuang, Z.; Chang, Y.-C.; Pao, C.-W.; Shao, Q.; Hu, Z.; Huang, X., Atomic-Thick Metastable Phase RhMo Nanosheets for Hydrogen Oxidation Catalysis, *Nat. Commun.,* 2023, **14**, 1761.

33 Yang, Y.; Sun, X.; Han, G.; Liu, X.; Zhang, X.; Sun, Y.; Zhang, M.; Cao, Z.; Sun, Y., Enhanced Electrocatalytic Hydrogen Oxidation on Ni/NiO/C Derived from a Nickel-Based Metal-Organic Framework, *Angew. Chem. Int. Ed.,* 2019, **58**, 10644-10649.

34 Zhou, Y.; Xie, Z.; Jiang, J.; Wang, J.; Song, X.; He, Q.; Ding, W.; Wei, Z., Lattice-Confined Ru Clusters with High CO Tolerance and Activity for the Hydrogen Oxidation Reaction, *Nat. Catal.,* 2020, **3**, 454-462.

35 Ghoshal, S.; Jia, Q.; Bates, M. K.; Li, J.; Xu, C.; Gath, K.; Yang, J.; Waldecker, J.; Che, H.; Liang, W.; Meng, G.; Ma, Z.-F.; Mukerjee, S., Tuning Nb-Pt Interactions To Facilitate Fuel Cell Electrocatalysis, *ACS Catal.,* 2017, **7**, 4936-4946.

36 Qiu, Y.; Xin, L.; Li, Y.; McCrum, I. T.; Guo, F.; Ma, T.; Ren, Y.; Liu, Q.; Zhou, L.; Gu, S.; Janik, M. J.; Li, W., BCC-Phased PdCu Alloy as a Highly Active Electrocatalyst for Hydrogen Oxidation in Alkaline Electrolytes, *J. Am. Chem. Soc.,* 2018, **140**, 16580-16588.

37 Wang, H.; Yang, Y.; DiSalvo, F. J.; Abruña, H. D., Multifunctional Electrocatalysts: Ru-M (M = Co, Ni, Fe) for Alkaline Fuel Cells and Electrolyzers, *ACS Catal.,* 2020, **10**, 4608-

4616.

38 Scofield, M. E.; Zhou, Y.; Yue, S.; Wang, L.; Su, D.; Tong, X.; Vukmirovic, M. B.; Adzic, R. R.; Wong, S. S., Role of Chemical Composition in the Enhanced Catalytic Activity of Pt-Based Alloyed Ultrathin Nanowires for the Hydrogen Oxidation Reaction under Alkaline Conditions, *ACS Catal.,* 2016, **6**, 3895-3908.

39 Qin, B.; Yu, H.; Jia, J.; Jun, C.; Gao, X.; Yao, D.; Sun, X.; Song, W.; Yi, B.; Shao, Z., A Novel IrNi@PdIr/C Core-Shell Electrocatalyst with Enhanced Activity and Durability for the Hydrogen Oxidation Reaction in Alkaline Anion Exchange Membrane Fuel Cells, *Nanoscale,* 2018, **10**, 4872-4881.

40 Hyun, J.; Pak, C., Facile Preparation of Core-Shell Ru@Ir/C Catalyst as a Bifunctional Electrocatalyst for Reversal-Tolerant Anode in Polymer Electrolyte Membrane Fuel Cell, *J. Power Sources,* 2025, **626**, 235716.